A Photoacoustic Transceiver Chipset with On-Chip Feature-Extraction RX and Pulse-Energy-Stabilized TX for Bio-Substance Quantification

Jianyu Zhang[1,2], Zhizhang Li[1,2], Kangkang Xu[1,2], Shuo Zhang[1,2], Shihong Zhou[1,2], Cheng Chen[1]*, Guoxing Wang[1]
[1]National Key Laboratory of Advanced Micro and Nano Manufacture Technology, Shanghai Jiao Tong University, China.
[2]School of Integrated Circuits (School of Information Science and Electronic Engineering), Shanghai Jiao Tong University, China. (Email: chencheng_sjtu@sjtu.edu.cn)

***Abstract*—This paper presents a Photoacoustic (PA) transceiver chipset for bio-substance quantification. The PA receiver (RX) integrates a peak-detect-and-sample-hold circuit (PDSH) for analog-domain amplitude-phase decoupling and a time-division-multiplexed cyclic-interpolated time-to-digital converter (TDM-CI-TDC) for hardware-efficient quantization, achieving RMS resolutions of 11.25 µV and 305.5 ps, respectively. The PA-dedicated pulsed-laser driver (TX) employs a pulse-frequency-modulated (PFM) DC-DC based energy bank and a pulse-width-stabilized delay-locked loop (DLL) to ensure laser pulse energy stability, generating pulses with tunable widths from 15.7 ns to 291.3 ns and <0.48% energy variation at 1 kHz pulse repetition frequency. Validated with glucose phantom test, the chipset demonstrates a linear response (R^2=0.9916) with nonlinearity error below 6.48% full scale.**

Keywords*—*photoacoustic, amplitude-phase extraction, high-stability pulsed-laser driver, bio-substance quantification

I. Introduction

Photoacoustic (PA) sensing has emerged as a promising biomedical modality, leveraging the mechanism of amplitude-phase dual modulation to enable low-concentration substance quantification, such as blood glucose or Na^+ [1][2]. As illustrated in Fig. 1a, this technique uniquely combines the chemical specificity of optical fingerprints with the deep tissue penetration of acoustic waves. Despite its potential for precision sensing, widespread adoption is hindered by the bulky nature of existing systems and the stringent performance requirements of the PA receiver (RX) and pulsed-laser driver (TX).

Unlike PA imaging, high-precision bio-substance quantification imposes more stringent RX requirements. Since physiological concentrations typically fluctuate within a narrow range, the system necessitates superior sensitivity to resolve concentration-induced PA variation at the µV-level for amplitude and ps-level for phase as shown in Fig. 1b. While conventional direct-sampling architectures scale well for multi-channel integration [3][4], they face a fundamental trade-off between power consumption and quantization precision. Although coherent detection techniques can enhance SNR, they need predefined signal templates, inevitably increasing system complexity [5][6]. Furthermore, given the high signal sparsity (<1% duty cycle), digitizing entire waveforms introduces significant data redundancy and processing overhead. On the TX side, as illustrated in Fig. 1c, a dedicated PA TX delivers high-energy pulses (µJ to mJ range) with tunable widths spanning tens to hundreds of nanoseconds to meet various pulse width constraints. Traditional PA excitation relies on discrete, bulky benchtop laser sources. Although these can provide sufficient energy, their large volume and high cost hinder PA system miniaturization. FET-controlled laser drivers, despite years of development and widespread use in LiDAR applications [7][8][9], have not been optimized for the stringent requirements of PA excitation. Recent capacitor-discharge-based PA TX designs achieve high efficiency [10], yet their fixed pulse widths restrict adaptability across different targets. Critically, any pulse-to-pulse energy variation is directly translated to noise in the PA signal, complicating downstream analysis and limiting quantification accuracy.

This work was supported by National Natural Science Foundation of China (Grant No. 62404134).

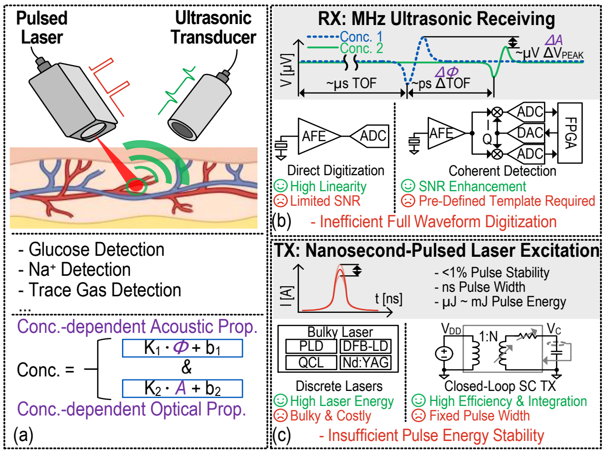

Fig. 1. Principle of the photoacoustic-based substance quantification and existing solutions for PA RX and TX.

II. Proposed Photoacoustic RX/TX Chipset

To address the aforementioned challenges, this work proposes a co-optimized PA transceiver chipset for seamless excitation-sensing synergy, as illustrated in its holistic architecture in Fig. 2. The RX employs analog-domain amplitude-phase decoupling with temporal quantization to eliminate data redundancy while maintaining high-precision voltage and time-domain resolution. The TX ensures pulse energy stability via a power-stabilized energy bank and a jitter-resilient, delay-lock-loop (DLL) based pulse generator for precise laser diode (LD) driving. The detailed circuit implementation and design considerations for each sub-block are elaborated in the following parts.

A. On-Chip Amplitude-Phase Decoupled RX

The RX architecture, illustrated in Fig. 3a, processes the AC-coupled input through an analog front-end (AFE) comprising two low-noise amplifiers (LNAs) and a programmable gain amplifier (PGA). A subsequent peak-detect-and-sample-hold (PDSH) decouples the amplified PA signal into its delay (Φ) and amplitude (A) features, which are sequentially digitized by a time-division-multiplexed cyclic-interpolated TDC (TDM-CI-TDC). Specifically, the TDC first quantizes Φ, followed by A via an integrated voltage-to-time converter (VTC). The AFE utilizes two current-feedback

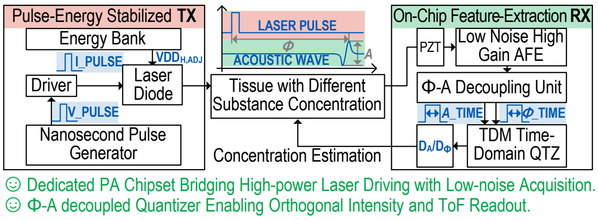

Fig. 2. Conceptual diagram of the proposed PA transceiver chipset.

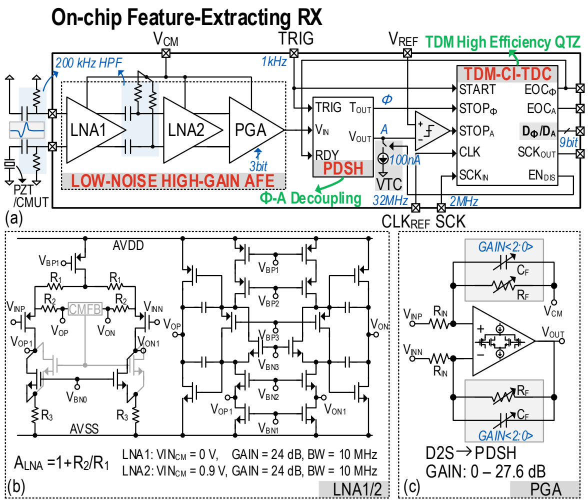

Fig. 3. System diagram of the proposed PA RX and schematic of the AFE.

LNAs to suppress active-load noise [11], with the first stage supporting a 0V input common mode voltage for passive PZT transducers as shown in Fig. 3b. Inter-stage AC coupling rejects low-frequency artifacts and prevents saturation. As illustrated in Fig. 3c, a resistive-feedback PGA with a complementary PN input pair maximizes input swing. The AFE provides 48–75.6 dB of tunable gain to accommodate PA signal variations driven by the TX.

The PDSH circuit, which is shown in Fig. 4a, implements a self-locking loop comprising a high-speed static comparator, a bootstrap switch (BS), and split sampling capacitors. Leveraging the intrinsic RC lag (τ) of the BS, the comparator triggers the locking phase at the crossover of the input and tracking signals as illustrated in Fig. 4c. This transition precisely captures the peak amplitude- A while simultaneously marking the arrival time-Φ, achieving reliable analog-domain Φ-A decoupling. By approximating the PA waveform near its peak as:

$$\mathrm{V}_{IN} = \mathrm{V}_{PEAK} - kt^2/2 \quad (1)$$

The locked voltage V_{LOCK} and peak-timing error ΔT_{PEAK} can be derived as:

$$\mathrm{V}_{LOCK} = \mathrm{V}_{PEAK} - k(\Delta \mathrm{T}_{PEAK})^2/2 - k\tau^2/2 + \mathrm{V}_{N,RMS} \quad (2)$$

$$\Delta \mathrm{T}_{PEAK} = \mathrm{T}_{DELAY} - (\mathrm{V}_{OS} + \mathrm{V}_{N,CMP})/k\tau \quad (3)$$

Where V_{OS} and T_{DELAY} represent the comparator's offset and propagation delay. These parameters can be optimized to improve the Φ-A acquisition accuracy significantly. To mitigate PA excitation-induced noise, a blanking module, as shown in Fig. 4b, masks the signal path for 2–4 μs post-trigger, preventing false locking and ensuring robust operation.

Fig. 5 illustrates the TDM-CI-TDC architecture, which utilizes a switched-frequency ring oscillator (SFRO)-based cyclic interpolator [12]. The TDC integrated a 12-bit coarse counter and two 4-bit interpolation fine counters. Driven by a

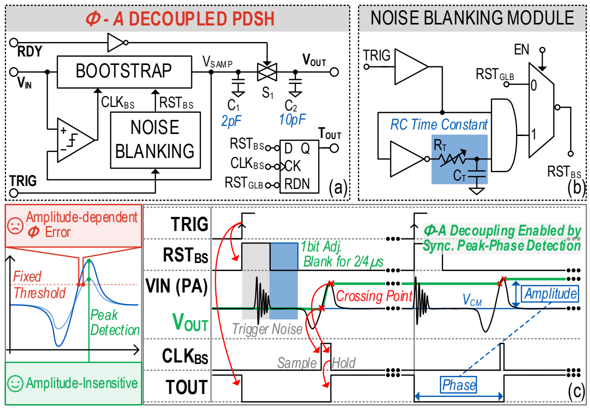

Fig. 4. System and timing diagram of the proposed Φ-A decoupled PDSH.

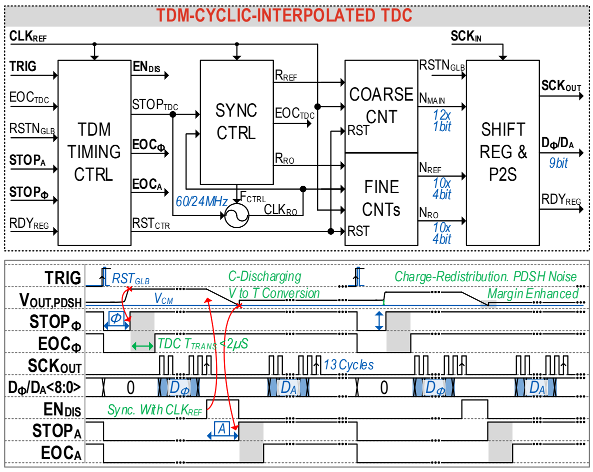

Fig. 5. Schematic and timing diagram of the proposed TDM-CI-TDC.

32 MHz reference clock, the 10-cycle interpolation quantization yields a 30.52 ps LSB across a 128 μs dynamic range. The TDM operation sequentially quantizes Φ and A. With the PA signal synchronized to the laser trigger, Φ is first resolved by leveraging the PDSH T_{OUT} as the TDC stop trigger. Subsequently, a synchronized 100-nA current source performs as a VTC by discharging the sampled peak voltage on C_2 in Fig. 4a, triggering the TDC for A quantization upon threshold crossover. Throughout this procedure, the split capacitor C_1 remains undischarged; its charge is redistributed in the following period to boost the comparator's negative input, thereby enhancing the noise margin. To optimize power and linearity, the SFRO employs inter-stage switches to eliminate standby intermediate states, achieving zero-static-power operation and a deterministic fixed-phase startup.

B. High Energy Efficiency Pulse-Energy-Stabilized TX

As illustrated in Fig. 6, the TX architecture optimizes LD pulse energy stability by precisely governing the drive pulse width and supply voltage. A 32-MHz charge-pump DLL, sharing its reference with the RX, locks the unit delay at 15.625 ns [13]. To ensure common-mode rejection and timing consistency, the DLL integrates a PSRR-enhanced bias generator and fully differential delay cells as detailed in Fig. 7a. An initial control unit is included to extend the locking range and prevent false-locking. Combined with a chopped-buffer-isolated delay array and 4-bit MUX, the TX generates stable, tunable pulse widths to precisely confine the laser pulse.

For supply voltage, a 5-18V PFM-based DC-DC converter leverages the low-duty-cycle nature of PA excitation for high

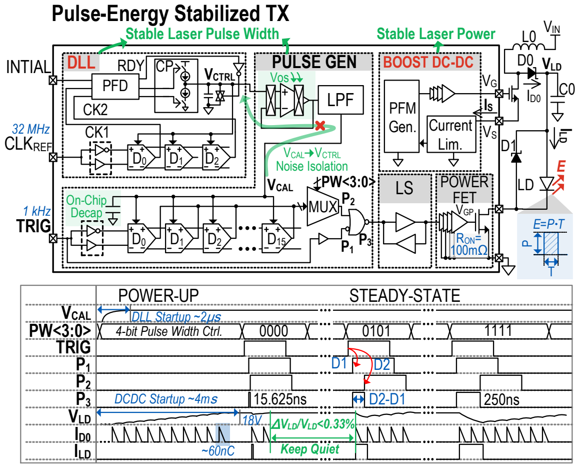

Fig. 6. System and timing diagram of the proposed PA TX.

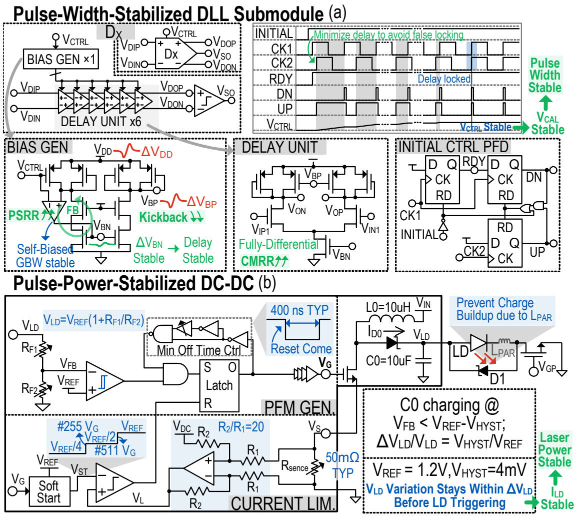

Fig. 7. Schematic of DLL submodule and PFM DC-DC converter.

efficiency which is detailed in Fig. 7b. The 1 MHz converter utilizes a 10 µH inductor L_0 and a 10 µF storage capacitor C_0. By limiting the peak charging current, it achieves a stable 60 nC charge delivery per cycle and a fine 6 mV voltage step. With a 4 mV-V_{HYST} and 1.2 V-V_{REF}, output stability is maintained within 0.33%. Loop stability is ensured by a 400-ns minimum off-time, while a digital soft-start circuit stages the current limit (1/4 and 1/2 over 255-cycle intervals) to suppress inrush current.

The LD is low-side driven by a 40-V LDMOS with 100mΩ R_{ON}. Optimized grounding between the level shifter and power FET minimizes ringing, ensuring reliable switching. Finally, a parallel reversed Schottky diode provides a fast discharge path to prevent LD from reverse-bias damage and sharpen pulse edges for an optimized PA excitation profile.

III. Measurement Results

The chipset was fabricated in a 180 nm BCD CMOS process, with active areas of 1.56 mm² (RX) and 4.16 mm² (TX) as shown in Fig. 8. Experimental validation utilized a 5 MHz PZT transducer (Doppler I2-5C10CF25) and a 905 nm LD (OSRAM SPL-TL90AT03). Fig. 9 summarizes the measured RX performance. The LNA1 achieves an input-referred noise of 1.48 nV/√Hz at 5 MHz, with a total AFE gain of 44.9-70.7 dB (Fig. 9a). The TDC interpolator exhibits a DNL/INL of [-0.6, 0.7] / [-2.3, 3.4] LSB as shown in Fig. 9b. The PDSH performance, characterized at 1.25 V and 1.55 V

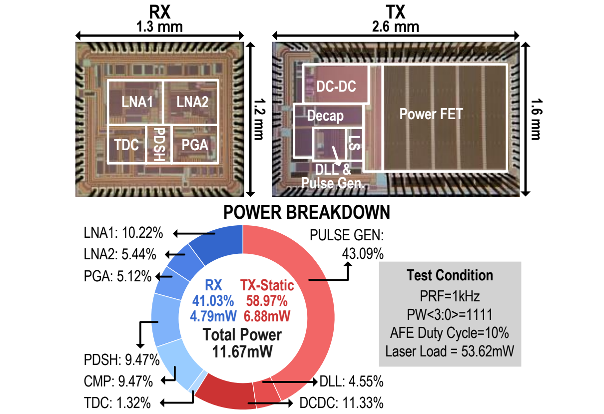

Fig. 8. Die photo of the proposed PA chipset and its power breakdown.

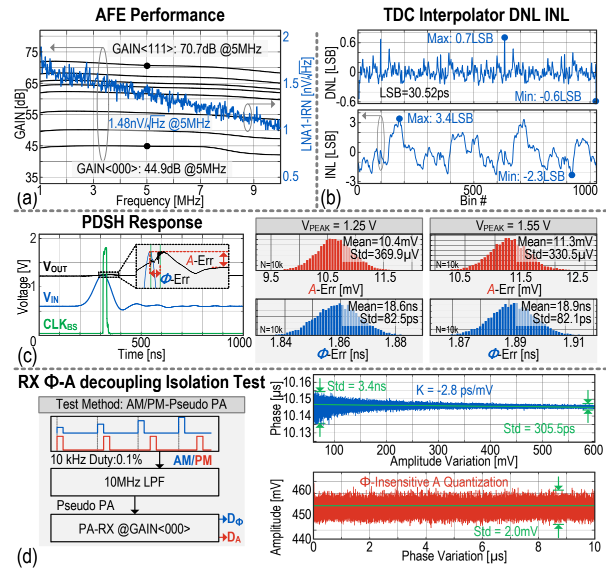

Fig. 9. Measurement results of the proposed RX.

peaks (Fig. 9c), demonstrates a mean amplitude error of <11.3 mV (<369.9 µV RMS) and a mean delay error of <18.9 ns (<82.5 ps RMS jitter). These conservative metrics include noise and offset contributions from the off-chip test buffer. The *Φ-A* quantization orthogonality of the entire RX was verified via amplitude-modulated (AM) and phase-modulated (PM) pseudo-PA signals (Fig. 9d). At a fixed input phase, the mean phase quantization remains highly stable across amplitude sweeps, exhibiting a minimal voltage-to-phase crosstalk slope of -2.8 ps/mV. The timing resolution naturally improves with SNR, reaching 305.5 ps RMS at 600 mV input. Conversely, phase variations show negligible impact on amplitude resolution, which remains consistent at 2mV RMS, corresponding to an input-referred resolution of 11.25 µV RMS.

Fig. 10 details the TX performance. The DC-DC recovers within 150µs under max LD loading (Fig. 10a). The DLL produces linear 4-bit adjustable pulses ranging from 15.7 ns to 291.3 ns with a minimum RMS jitter of 124 ps (Fig. 10b). The TX-excited laser pulses were captured by a high-speed PD (Hamamatsu G8370-81), and amplified by a TIA. The induced PA signals were amplified by RX-AFE. These waveforms, along with the drive signal V_{GP}, were recorded by a high-speed oscilloscope (LeCroy WaveRunner 8404) as shown in Fig. 10c. To evaluate energy stability, captured laser waveforms were integrated within the pulse window. The RMS stability variation is 0.48% at the narrowest 15.7 ns pulse and improves to 0.13% for wider configurations. Finally, glucose phantom

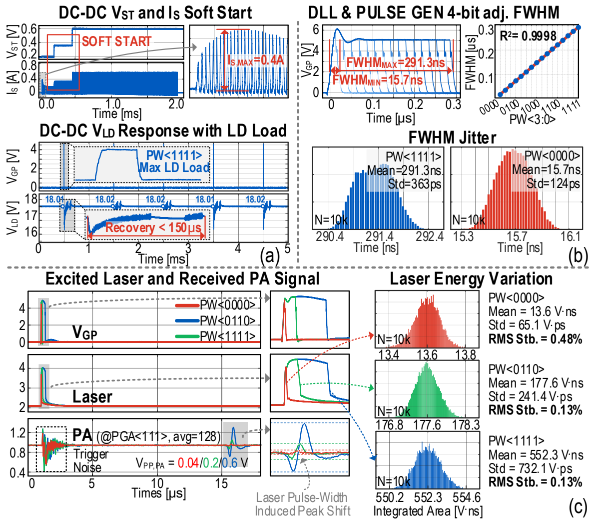

Fig. 10. Measurement results of the proposed TX.

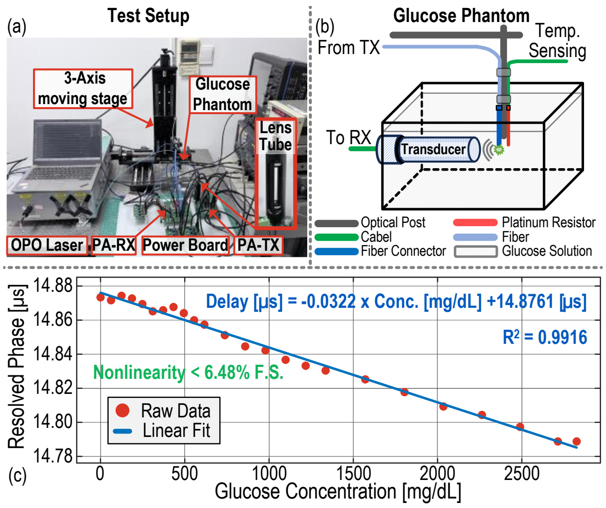

Fig. 11. Glucose phantom test setup and fitting results.

TABLE I. COMPARISION WITH STATE-OF-THE-ART PA RX/TX

	Parameter	This Work	ISSCC 2025[3]	ISSCC 2017[4]	TbioCAS 2021[5]	TbioCAS 2019[6]
RX Performance	Technology[nm]	180	65	28	65	65
	Area[mm^2]	1.560	0.118	0.065	5.710	0.600
	Application	**PA Bio-Substance Quantification**	PA Imaging	PA Imaging	PA Imaging	PA Imaging /Temp.
	Power[mW]	**4.79[a]**	5.83	26.70	115.20	20.00
	Transducer Type	PZT	PZT	CMUT	PZT	PZT
	Center Freq.[MHz]	5.0	3.5	5.0	1.0	1.0
	IRN[nV/$\sqrt{Hz}$]	**1.48**	3.50	N/A	N/A	1.58
	RMS Phase Precision[ps]	**305.5**	14100	2400	28900	2800
	RMS Amplitude Precision[μV]	11.25[b]	6.08[c]	N/A	0.18	50.00
	Output Data	**Extracted Features (A, Φ)**	Raw waveform			
TX Performance	Parameter	This Work	ESSERC 2025[10]	JSSC 2025[7]	JSSC 2023[8]	JSSC 2023[9]
	Application	**PA Bio-Substance Quantification**	PA Imaging	LiDAR	LiDAR	LiDAR
	Technology[nm]	180	180	180	180	250
	Area[mm^2]	4.160	6.125	2.340	13.440	1.080
	Static Power[mW]	**6.88**	N/A	N/A	32.98[d]	N/A
	Pulse Width[ns]	**15.7-291.3**	~200	0.1-2.0	0.36-2.06	N/A
	PRF	**1k-5kHz**	1kHz	30MHz	10MHz	5MHz
	Input Voltage[V]	5	5	20	1.8	4-40
	Bus Voltage[V]	18	33	20	12.5	60-80
	Driver Type	FET Controlled	Capacitive Discharge	Double-Pulse Overlapping	FET Controlled	Capacitive Discharge
	Laser Diode Type	EEL	EEL	EEL	VCSEL	N/A
	Pulse Stability	**<0.48%**	N/A	N/A	N/A	N/A

[a] Measured at 1 kHz with AFE duty cycle of 10%.
[b] Calculated by: $V_{OUT,rms}/Gain_{AFE}$ @PGA<000>.
[c] Calculated by: $V_{FS,rms}/(10^{DR/20} \times Gain)$.
[d] DLL, Pulse Gen, Bias, LDO.

experiments were conducted to validate the proposed PA chipset as shown in Fig 11. Over a concentration range of 0 to 2825 mg/dL, the system demonstrates exceptional linearity, achieving a coefficient of determination (R^2) of 0.991 between PA phase and glucose concentration and nonlinearity error below 6.48% full scale despite weak amplitude modulation at 905 nm.

As summarized in Table I, the RX achieves a >7-fold improvement in phase resolution compared to state-of-the-art works while enabling direct analog-domain features extraction and quantization to minimize data redundancy. The TX provides excellent pulse energy stability and a wider tunable pulse-width range, accommodating diverse sensing scenarios and ensuring high-fidelity excitation for bio-substance quantification.

IV. CONCLUSION

The proposed PA transceiver chipset provides a co-optimized solution for bio-substance sensing. The RX adopts on-chip Φ-A decoupling and a TDM-CI-TDC to achieve µV-level amplitude and ps-level phase feature quantization. The TX incorporates a DLL-based pulse generator and a PFM DC-DC converter to ensure stable laser excitation with a minimal energy variation. Validated by glucose phantom test, this work demonstrates its potential for miniaturized, non-invasive PA bio-substance quantification.

REFERENCES

[1] N. Uluç et al., " Non-invasive measurements of blood glucose levels by time-gating mid-infrared optoacoustic signals," *Nature Metabolism*., vol. 6, pp. 678–686, Apr. 2024.

[2] J. Li et al., "Non-invasive, real-time monitoring of blood Na^+ in vivo using terahertz optoacoustics," *Optica*, vol. 12 , pp. 914–923, Jul. 2025.

[3] H. -C. Liao *et al.*, "35.2 A Spatial-Domain Compressive-Sensing Photoacoustic Imager with Matrix-Multiplying SAR ADC," *2025 IEEE International Solid-State Circuits Conference (ISSCC)*, San Francisco, CA, USA, 2025, pp. 1-3.

[4] M. -C. Chen *et al.*, "27.5 A pixel-pitch-matched ultrasound receiver for 3D photoacoustic imaging with integrated delta-sigma beamformer in 28nm UTBB FDSOI," *2017 IEEE International Solid-State Circuits Conference (ISSCC)*, San Francisco, CA, USA, 2017, pp. 456-457.

[5] C. Yang *et al.*, "A Super-Sensitivity Photoacoustic Receiver System-on-Chip Based on Coherent Detection and Tracking," in *IEEE Transactions on Biomedical Circuits and Systems*, vol. 15, no. 3, pp. 454-463, June 2021.

[6] Z. Fang *et al.*, "A Digital-Enhanced Chip-Scale Photoacoustic Sensor System for Blood Core Temperature Monitoring and In Vivo Imaging," in *IEEE Transactions on Biomedical Circuits and Systems*, vol. 13, no. 6, pp. 1405-1416, Dec. 2019.

[7] Z. Tong, J. Huang, X. Mao, R. P. Martins and Y. Lu, "A Double Pulse Overlapping Laser Diode Driver With Minimum 100-ps Pulse for LiDAR System," in *IEEE Journal of Solid-State Circuits*, vol. 60, no. 2, pp. 555-567, Feb. 2025.

[8] S. Zhuo *et al.*, "Solid-State dToF LiDAR System Using an Eight-Channel Addressable, 20-W/Ch Transmitter, and a 128 × 128 SPAD Receiver With SNR-Based Pixel Binning and Resolution Upscaling," in *IEEE Journal of Solid-State Circuits*, vol. 58, no. 3, pp. 757-770, March 2023.

[9] S. -Y. Li *et al.*, "A 4–40 V Wide Input Range Boost Converter With the Protection Re-Cycling Technique for 200 W High Power LiDAR System in a Long-Distance Object Detection," in *IEEE Journal of Solid-State Circuits*, vol. 58, no. 7, pp. 1850-1859, July 2023.

[10] D. Lin, M. Xu, Y. Liu, Y. Mao, F. Gao and Y. Gao, "A 5V Input Pulse-Charge-Regulated 46µJ/Cycle Laser Diode Driver with a Reconfigurable Switched-Capacitor Charger for Portable Photoacoustic Imaging," *2025 IEEE European Solid-State Electronics Research Conference (ESSERC)*, Munich, Germany, 2025, pp. 385-388.

[11] S. -J. Jung, S. -K. Hong and O. -K. Kwon, "Low-Power Low-Noise Amplifier Using Attenuation-Adaptive Noise Control for Ultrasound Imaging Systems," in *IEEE Transactions on Biomedical Circuits and Systems*, vol. 11, no. 1, pp. 108-116, Feb. 2017.

[12] P. Keränen and J. Kostamovaara, "A Wide Range, 4.2 ps(rms) Precision CMOS TDC With Cyclic Interpolators Based on Switched-Frequency Ring Oscillators," in *IEEE Transactions on Circuits and Systems I: Regular Papers*, vol. 62, no. 12, pp. 2795-2805, Dec. 2015.

[13] J. G. Maneatis, "Low-jitter process-independent DLL and PLL based on self-biased techniques," in *IEEE Journal of Solid-State Circuits*, vol. 31, no. 11, pp. 1723-1732, Nov. 1996.